Applied Physics Letters

Anomalous wavefront control via nonlinear acoustic metasurface through second-harmonic tailoring and demultiplexing

Cite as: Appl. Phys. Lett. **121**, 201703 (2022); https://doi.org/10.1063/5.0101076
Submitted: 29 May 2022 • Accepted: 27 October 2022 • Published Online: 15 November 2022

Zhenkun Lin, Yuning Zhang, K. W. Wang, et al.

AIP Publishing

Applied Physics Letters ARTICLE scitation.org/journal/apl

Anomalous wavefront control via nonlinear acoustic metasurface through second-harmonic tailoring and demultiplexing

Cite as: Appl. Phys. Lett. **121**, 201703 (2022); doi: 10.1063/5.0101076
Submitted: 29 May 2022 · Accepted: 27 October 2022 ·
Published Online: 15 November 2022

Zhenkun Lin, Yuning Zhang, K. W. Wang, and Serife Tol[a)]

AFFILIATIONS

Department of Mechanical Engineering, University of Michigan, Ann Arbor, Michigan 48109-2125, USA

Note: This paper is part of the APL Special Collection on Acoustic and Elastic Metamaterials and Metasurfaces.
[a)]**Author to whom correspondence should be addressed:** stol@umich.edu

ABSTRACT

We propose a nonlinear acoustic metasurface concept by exploiting the nonlinearity of locally resonant unit cells formed by curved beams. The analytical model is established to explore the nonlinear phenomenon, specifically the second-harmonic generation (SHG) of the nonlinear unit cell, and validated through numerical and experimental studies. By tailoring the phase gradient of the unit cells, nonlinear acoustic metasurfaces are developed to demultiplex different frequency components and achieve anomalous wavefront control of SHG in the transmitted region. To this end, we numerically demonstrate wave steering, wave focusing, and self-bending propagation. Our results show that the proposed nonlinear metasurface provides an effective and efficient platform to achieve significant SHG and separate different harmonic components for wavefront control of individual harmonics. Overall, this study offers an outlook to harness nonlinear effects for acoustic wavefront tailoring and develops potential toward advanced technologies to manipulate acoustic waves.

Engineered material systems have been widely used in controlling acoustic/elastic waves due to their unique and intriguing properties, such as bandgap and ability to slow the wave speed, which leads to diverse applications, including vibration suppression systems,[1,2] energy harvesting devices,[3,4] topological insulators,[5] and nonreciprocal wave propagation.[6,7]

Recently, phase-modulated metasurfaces[8] have gained increasing research interest due to their ability to control low-frequency waves with compact and lightweight structures. A metasurface is a thin layer in the host medium composed of an array of subwavelength-scaled features, which can introduce an abrupt phase shift in the wave propagation path and tailor the wavefront based on generalized Snell's law. The first studies on metasurface designs rely on linear properties of the unit structures to modulate the acoustic/elastic wavefront.[9–13] For instance, metasurface designs based on Helmholtz-resonator[14] or coiling-up space structure[9] were proposed to control the acoustic wavefront of reflected and transmitted waves. To enhance wave control opportunities beyond conventional linear metasurfaces, researchers have recently introduced nonlinearity in the acoustic metasurface designs and achieved extraordinary wave controllability. For example, Popa and Cummer[15] presented a single-layer structure with Helmholtz-resonators and nonlinear electronic circuits to achieve the second-harmonic generation (SHG) for nonreciprocal wave propagation. Guo *et al.*[16,17] proposed nonlinear acoustic metasurfaces based on mass-spring and rotating-square structures and explored SHG in the reflected region, revealing that the local resonance effects can amplify SHG.

Although promising, the current nonlinear acoustic metasurface studies mainly focus on generating and maximizing the higher-order harmonics. Yet, the phase modulation and wavefront control capability of these structures have not been explored in the acoustic regime. In addition, the resulting scattered wavefields often comprise a mixture of different harmonic components, which may weaken the efficiency of controlling them individually.

In this paper, we advance the state of the art by introducing a nonlinear acoustic metasurface for simultaneous higher-harmonic generation and unconventional wavefront manipulation. We examine the amplitude-dependent behavior of the SHG, and the phase modulation capability of the proposed metasurface, proving that it can effectively generate second-harmonic wave and simultaneously modulate its wavefront for various functions, including wave deflecting, wave focusing, and self-bending propagation, without influencing the propagation of fundamental wave components.

The proposed nonlinear acoustic metasurface concept is depicted in Fig. 1(a), which is composed of an array of sub-wavelength unit cells, consisting of three lumped masses coupled via two curved beams. The unit cell has a length of $l = 50.8$ mm, a width of $b = 50.8$ mm, and a thickness of $t = 100$ mm (parameters are detailed in the supplementary material, Table S1). We design the metasurface to control the acoustic wave propagating in air with mass density $\rho = 1.29$ kg/m^3 and sound speed $c = 340$ m/s. We focus on the problem of acoustic wave transmission when a plane wave at a single frequency normally impinges on the left lumped mass, m_1, and propagates through the metasurface. To analytically formulate the problem, we establish a simplified mass-spring-damper system, where the mass of the metasurface unit is assumed to be concentrated at the three lumped masses m_1, m_2, and m_3, and each curved beam is modeled as an ideal nonlinear spring with damping, as shown in Fig. 1(b).

Without loss of generality, the restoring forces of the nonlinear springs are assumed of the form, $F_i^{NL}(\Delta l) = k_i\Delta l + \alpha_i k_i \Delta l^2 + \beta_i k_i \Delta l^3, i = 1, 2$, where Δl is the deformation of the nonlinear springs, and k_i, α_i, and β_i are the stiffness parameters. These stiffness parameters are determined through the results from quasi-static analysis conducted in COMSOL Multiphysics (see the supplementary material, Sec. S2 for detailed description), yielding $k_1 = 2.78 \times 10^5$ N/m, $\alpha_1 = 2.00 \times 10^3$ m^{-1}, $\beta_1 = 2.30 \times 10^6$ m^{-2}, $k_2 = 6.99 \times 10^5$ N/m, $\alpha_2 = -510$ m^{-1}, and $\beta_2 = 1.02 \times 10^6$ m^{-2}. We select the mass values $m_1 = 9.4$ g, $m_2 = 19.0$ g, and $m_3 = 6.0$ g, resulting in a system with two non-zero natural frequencies satisfying $f_2 = 2f_1 = 2$ kHz. It is pointed out in previous studies[16,17] that under such doubling resonance frequency condition, i.e., $f_2 = 2f_1$, the SHG can be maximized when the system is excited at f_1.

We assume a longitudinal wave with plane stress-wave field $\sigma_{inc}(x,t) = \sigma_0 \sin\left(2\pi f\left(t - \frac{x}{c}\right)\right)$ normally incident from the left-hand side of the metasurface unit along the positive x-direction, where σ_0 is the amplitude of the incident wave and the incident frequency is set to be $f = f_1 = 1$ kHz. Accordingly, the reflected and transmitted stress-wave fields, σ_{ref} and σ_{tr}, can be written as follows:

$$\sigma_{ref} = \sigma_{inc} + \rho c \frac{\partial u}{\partial t}, \quad \sigma_{tr} = -\rho c \frac{\partial u}{\partial t}, \tag{1}$$

where $u(x, t)$ is the resulting displacement field in the air. m_1 and m_3 are located at $x = 0$ and $x = l$, respectively. Then, the effective forces applied at m_1 and m_3 can be determined by matching the boundary conditions at the interfaces, i.e., $F_1 = -(\sigma_{inc}|_{x=0} + \sigma_{ref}|_{x=0})S$ and $F_3 = \sigma_{tr}|_{x=l}S$, where $S = bt$ is the area of the flat surfaces contacting air. As such, the governing equations of the metasurface unit can be expressed as follows:

$$m_1\frac{d^2u_1}{dt^2} = -\left(2\sigma_0 \sin(2\pi f t) + \rho c\frac{du_1}{dt}\right)S - F_1^{NL}(u_1 - u_2) - \eta_1\frac{d(u_1 - u_2)}{dt}, \tag{2a}$$

$$m_2\frac{d^2u_2}{dt^2} = F_1^{NL}(u_1 - u_2) + \eta_1\frac{d(u_1 - u_2)}{dt} - F_2^{NL}(u_2 - u_3) - \eta_2\frac{d(u_2 - u_3)}{dt}, \tag{2b}$$

$$m_3\frac{d^2u_3}{dt^2} = -\rho cS\frac{du_3}{dt} + F_2^{NL}(u_2 - u_3) + \eta_2\frac{d(u_2 - u_3)}{dt}, \tag{2c}$$

where u_1, u_2, and u_3 are the displacements of m_1, m_2, and m_3, respectively. η_1, η_2 are the damping coefficients of the two nonlinear springs. Then, Eq. (2) is solved analytically by adopting the Harmonic Balance Method (HBM) with the solutions u_i $(i = 1, 2, 3)$ assumed as

$$u_i(t) = u_i^0 + \sum_{n=1}^{N}\left[C_i^n \cos(2\pi n f t) + S_i^n \sin(2\pi n f t)\right], \tag{3}$$

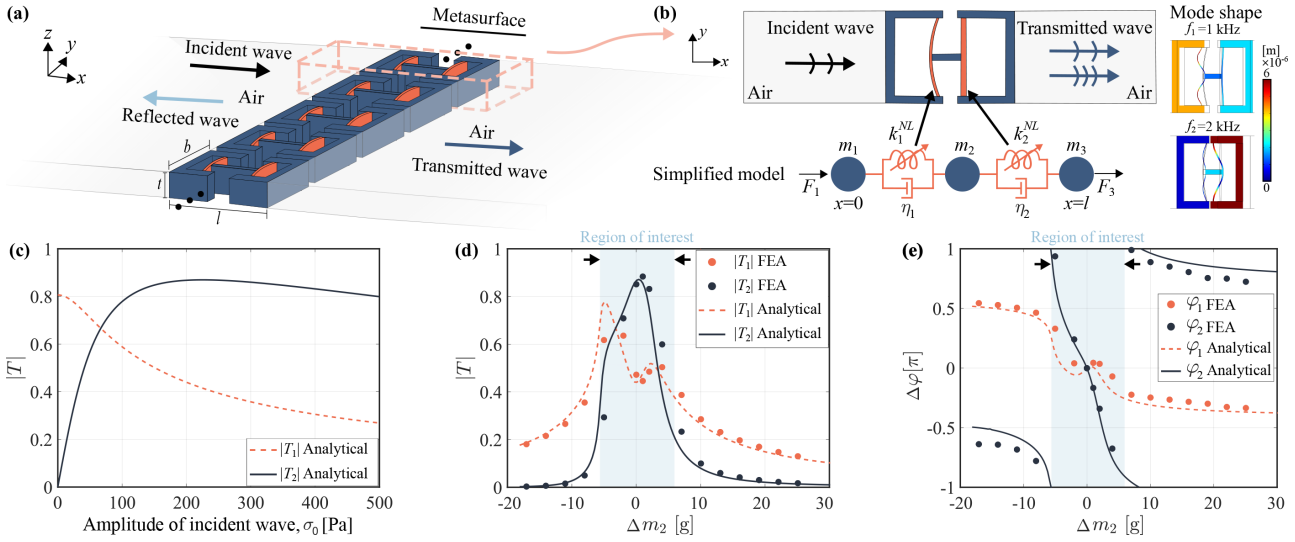

FIG. 1. Schematic of the (a) nonlinear acoustic metasurface and (b) unit cell. The inset in (b) depicts the mode shapes of the unit cell when $f_2 = 2f_1 = 2$ kHz. (c) The transmission ratios of both fundamental component ($|T_1|$) and SHG ($|T_2|$) under different amplitudes of the incident wave. (d) The transmission ratios and (e) phase modulation curve of fundamental wave component (φ_1) and SHG (φ_2) vary with the middle mass value deviating from 19 g, i.e., $\Delta m_2 = m_2 - 19$ g. The phase shift value with $m_2 = 19$ g is taken as the reference.

where u_i^0 represents the constant terms, C_i^n and S_i^n are the amplitudes of the sinusoidal terms, cosine and sine, respectively, and N is the number of harmonics truncated. By substituting Eq. (3) into Eq. (2) and matching the coefficients for different harmonics, we obtain a set of nonlinear equations with respect to the unknown coefficients u_i^0, C_i^n, and S_i^n, which can be numerically solved by the Newton–Raphson method.[18] Then, the complex transmission coefficients of each harmonic component can be obtained by substituting Eq. (3) into Eq. (1) and taking the ratio between the complex amplitudes of each harmonic and incident wave, yielding

$$T_n = \frac{2\pi n f \rho c}{\sigma_0}(C_3^n - jS_3^n), \quad n = 1, 2, \ldots, N, \tag{4}$$

where j is the imaginary unit. As such, the transmission ratio, $|T_n|$, of the n^{th} order harmonics and the corresponding phase shift caused by the metasurface unit, φ_n, can be calculated by taking the magnitude and angle of T_n, respectively (see the supplementary material, Sec. S3 for detailed derivation).

With this analytical model, we investigate the transmission ratio and phase shift of the undamped metasurface unit cell, as depicted in Figs. 1(c)–1(e). We first explore the amplitude-dependent behavior of the metasurface unit under different incident amplitudes, σ_0. As shown in Fig. 1(c), the fundamental wave component (f_1) dominates the transmitted wavefield when $\sigma_0 \approx 0$ Pa, indicating a nearly linear response. As σ_0 increases, the nonlinear effect occurs, leading to gradually enhanced SHG. The transmission ratio of SHG tends to saturate and reaches a maximal value of 0.84 when $\sigma_0 \approx 200$ Pa. Note that the transmission ratios of the third and higher-harmonic components are negligible ($|T_{n\geq 3}| < 0.005$) compared to fundamental and second-harmonic components, and most of the acoustic energy is converted to the SHG. Hence, the proposed unit cell provides an effective and efficient platform for SHG. The mechanism for the significant SHG in the transmitted region can be further interpreted by examining the mode shapes of the unit cell, as shown in the inset of Fig. 1(b). It is observed that m_3 has a large motion in the second resonant mode, i.e., f_2, while m_1 remains almost steady, indicating that the second-harmonic wave tends to propagate into the transmitted region instead of being reflected.

Moreover, we explore the unit cell's capability to modulate the wave transmission characteristics by tuning its parameters, specifically, m_2. We vary m_2 around 19 g ($m_2 = 19$ g $\pm\Delta m_2$) and set $\sigma_0 = 200$ Pa for higher SHG. Figure 1(d) shows that the transmission ratios of fundamental and second-harmonic components change dramatically with different m_2 due to the shift in natural resonances of the unit cell. As expected, the maximum SHG occurs when $\Delta m_2 = 0$ g, i.e., when $f_2 = 2f_1$. Apart from the transmission ratios, the phase modulation capability is another key factor in metasurface design. The phase shift should span the range from $-\pi$ to π in order to effectively control the acoustic field. As shown in Fig. 1(e), our design can introduce different phase shifts for the fundamental and second-harmonic waves by tailoring m_2, indicating the feasibility to achieve diverse wavefront control over different harmonic components. It is observed that the phase shift curve of the SHG covers the entire 2π phase range, revealing that any type of anomalous wavefront control over the SHG can be realized, while the phase shift of the fundamental component is insensitive to the change of m_2 in the range of interest. The mechanism for the negligible phase shift of the fundamental component can be interpreted by examining the mode shape of the unit cell, as shown in the inset of Fig. 1(b), where m_2 remains almost steady in the first resonant mode, i.e., f_1, indicating that m_2 can be treated as a vibration node. Hence, varying m_2 have limited effects on the dynamic responses of the system. This interesting phenomenon is utilized in the following metasurface designs to split the SHG from the fundamental component for individual control.

Furthermore, we conduct the finite element analysis (FEA) in COMSOL Multiphysics. A 2D model is developed to calculate the vibro-acoustic response of the unit cell under a planar-type background pressure field at 1 kHz in the incident region. The interfaces between unit cell structure and air are set as acoustic-structure boundary to include acoustic-vibration coupling, and the perfectly matched layers (PMLs) are implemented at the ends to avoid the reflection. The transmission ratios and phase shifts of both harmonics are obtained in Figs. 1(d) and 1(e), respectively, and demonstrate an excellent agreement with the analytical solutions.

Next, we demonstrate the applicability of the proposed concept with a prototypical unit cell example. The unit cell is fabricated and experimentally tested for its transmission properties featuring a SHG with a tailorable desired phase shift. The mass blocks are fabricated through Form 3 SLA 3D Printer and connected via curved beams made of 1095 spring steels. The stiffness parameters of the curved beams are tested through tensile testing machines, yielding $k_1 = 2.60 \times 10^4$ N/m, $\alpha_1 = 3.84 \times 10^3$ m^{-1}, $\beta_1 = 8.53 \times 10^5$ m^{-2}, $k_2 = 3.28 \times 10^4$ N/m, $\alpha_2 = 141$ m^{-1}, and $\beta_2 = 1.03 \times 10^3$ m^{-2}. Accordingly, the mass values $m_1 = 14.42$ g, $m_2 = 7.35$ g, and $m_3 = 7.65$ g are selected to guarantee the second natural frequency doubles the fundamental one, i.e., $f_1 = f_2/2 = 266.4$ Hz. The metasurface unit cell is hung with soft rubber bands, as depicted in Fig. 2(a). A circular magnet with 12.7 mm diameter is bonded at the center of m_1. The excitation signal is generated by the waveform generator (Agilent 33522A) and sent to an electromagnet copper magnetic coil through an amplifier (TREK PZD350A) to apply tunable harmonic forces to m_1. We measure the out-of-plane velocity of m_3 via Polytec PSV-500 scanning laser Doppler vibrometer (LDV) to obtain the transmitted waves, as demonstrated in the inset of Fig. 2(a), and apply the fast Fourier transformation technique to obtain the amplitudes and phase shift variation of fundamental and second-harmonic components.

To characterize the amplitude-dependent behavior of our experimental prototype, we tune the voltage in the signal generator and record the transmitted wave under the same excitation frequency $f = f_1 = 266.4$ Hz, as plotted in Fig. 2(b). The results verify that it can realize significant SHG in the transmitted region, and higher input voltage leads to a larger ratio between the velocity amplitudes of SHG and the fundamental component (v_2/v_1), indicating that more energy is converted into SHG as the system nonlinearity increases. In addition, we measure the velocity response and phase variation of the right mass block, m_3, under different middle mass value around $m_2 = 7.35$ g with the same excitation, as presented in Figs. 2(c) and 2(d). The SHG is maximized when $\Delta m_2 = 0$ g, which corresponds to the arrangement with $f = f_1 = f_2/2 = 266.4$ Hz. Meanwhile, a local drop is observed in the fundamental wave velocity around the peak of SHG since more energy is transformed into SHG around this region. Also, the nonlinear unit cell can introduce different phase shifts into the generated second-harmonic wave by varying m_2, as shown in Fig. 2(d). Changing m_2 has larger effect on the phase variation of SHG relative to the fundamental component, which agrees with our previous discussions.

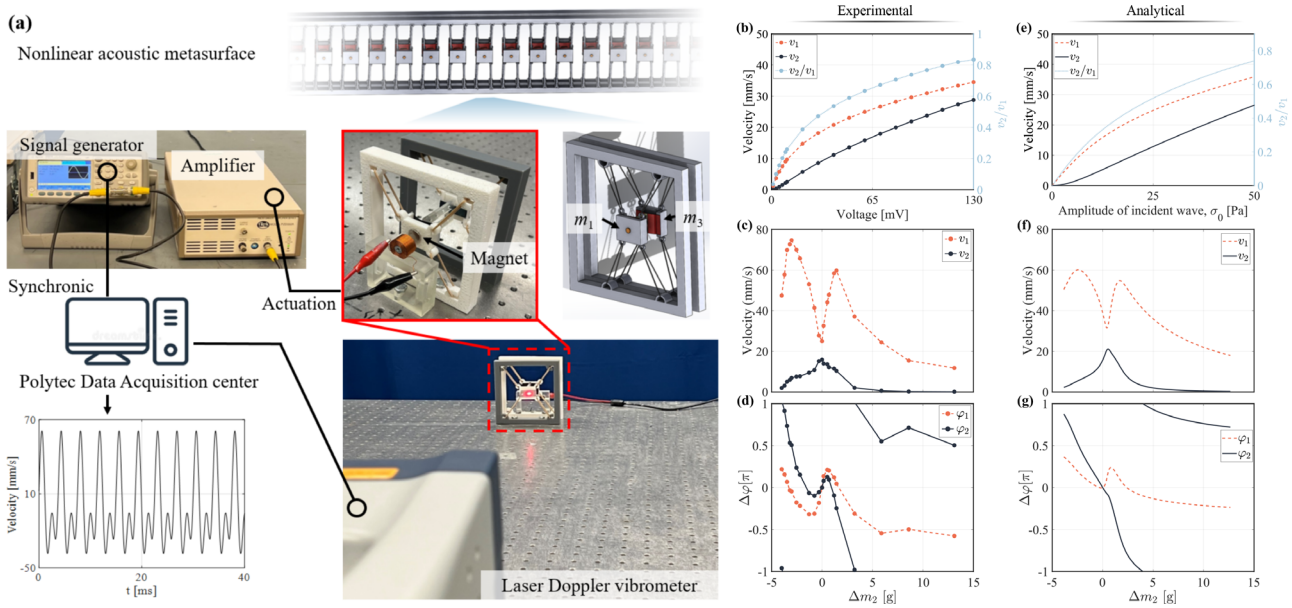

FIG. 2. (a) The nonlinear acoustic metasurface and the unit cell experimental configuration. (b)–(g) Comparison between the experimental and analytical velocity responses under harmonic excitation at $f = f_1 = 266.4$ Hz. (b) Measured velocity of m_3 under different voltage inputs. (c) Measured velocity responses and (d) phase shift variation under different middle mass value around 7.35 g, $\Delta m_2 = m_2 - 7.35$ g, and fixed voltage 60 mV. The phase shift value with $m_2 = 7.35$ g is taken as reference for phase variation plot. (e) Analytical prediction of the amplitude-dependent response with experimentally measured curved beam parameters. (f) Analytical velocity responses and (g) phase shift variation with incident amplitude $\sigma_0 = 40$ Pa and damping coefficients $\eta_1 = \eta_2 = 0.15$ under different m_2, demonstrating a similar trend to experimental results, as shown in (c) and (d).

In addition, Figs. 2(e)–2(g) show the corresponding analytical results with the experimentally measured structural parameters and proper selection of incident amplitude and damping coefficients. Our experimental results and the analytical solutions match each other well in terms of the amplitude-dependent behavior and the modulation of the transmission characteristics, revealing that our experimental prototype can be utilized to provide an excellent physical implementation of the proposed unit cell for SHG and wave manipulation.

Having the analytical model of the nonlinear unit cell validated through numerical simulations and the concept of generating significant higher order harmonics with phase-shift features realized and verified by experiments, we design acoustic metasurfaces to manipulate the wavefront of the transmitted wavefield based on the phase shift profiles in Fig. 1(e). The designed metasurface consists of an array of 25 units with a gap of 2 mm. By tailoring the middle mass value m_2 along the metasurface, we present different metasurfaces to control the normally incident acoustic wave at 1 kHz and achieve full wavefront control of the SHG. In all metasurface designs, the propagating direction of the fundamental wave remains almost unchanged since most of the metasurface units introduce a constant phase shift, i.e., $d\varphi_1/dy \approx 0$, where y represents the vertical coordinates with the origin located at the center of the metasurface, while the SHG will be split from the fundamental component for various types of anomalous wavefront control. The performance of the proposed metasurfaces is validated via finite element simulations conducted in COMSOL Multiphysics. The incident wave is generated by applying a planar-type background pressure field at 1 kHz, and the model is surrounded by the PML to simulate the infinite acoustic domain, as depicted in Fig. 3(a). Note that the simulations do not account for air inside the nonlinear unit cells, which has a negligible damping effect on the acoustic-induced vibrations of the nonlinear beams. Hence, it does not impact the overall wavefront tailoring performance of the nonlinear metasurface as presented with three numerical case studies. The first type of nonlinear metasurface is designed to demultiplex different frequency components in the transmitted region by guiding the SHG in different desired angles, θ_2, according to the design principle based on the generalized Snell's law: $\varphi_2(y) = -yk_2 \sin\theta_2$, where k_2 is the wavenumber of the second-harmonic component. To this end, we design three metasurfaces with theoretical deflecting angles of $\theta_2 = 30°$, $\theta_2 = 45°$, and $\theta_2 = 60°$ for the second-harmonic wave. Figures 3(b)–3(d) show the resulting scattered acoustic pressure fields in the transmitted region, where significant SHG is realized and the incident waves are split into two beams as designed. One beam maintains the original propagating direction with the same wavelength as the incident wave (i.e., the fundamental wave component). The other is deflected by the desired angle, θ_2, and propagates with half of the original wavelength (i.e., the second-harmonic component). Therefore, the proposed metasurfaces can simultaneously achieve significant SHG and frequency demultiplexing.

Aside from deflecting metasurface, the focusing metasurface is of particular interest in engineering applications requiring localized high-intensity wave energy. To focus the SHG at (f_x, f_y) away from the center of the metasurface, a hyperbolic-type phase profile $\varphi_2(y) = k_2\left(\sqrt{f_x^2 + (y - f_y)^2} - \sqrt{f_x^2 + f_y^2}\right)$ is required to form a semicircle equiphase surface in the transmitted region.[19] We first demonstrate a

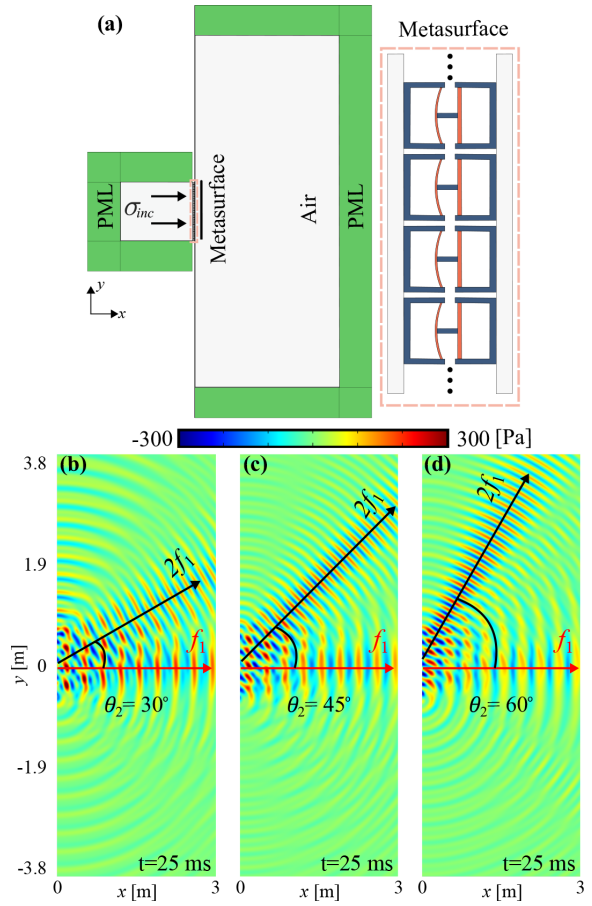

FIG. 3. (a) Schematic of the nonlinear acoustic metasurface placed in the air. The transmitted acoustic pressure fields of deflecting metasurfaces with desired angle: (b) $\theta_2 = 30^\circ$, (c) $\theta_2 = 45^\circ$, and (d) $\theta_2 = 60^\circ$.

focusing metasurface design to localize the SHG at (f_x, f_y)=(304.8, 304.8) mm. The transmitted acoustic pressure field is shown in Fig. 4(a), and the root mean square (RMS) acoustic pressure results are calculated and normalized by the incident acoustic pressure as plotted in Fig. 4(b). The maximum acoustic pressure intensity occurs at (306, 300) mm with only (0.39%, 1.57%) deviation away from the desired focal point, and the acoustic pressure is amplified by 2.12 times in the focal area. Hence, the nonlinear focusing metasurface can focus the SHG at the desired region, offering great potential in imaging small objects for various applications (such as bio-medical or structural health monitoring). In addition, the performance of the metasurface is examined to focus the SHG at a further point $(f_x, f_y) = (609.6, 609.6)$ mm, close to the upper boundary of the metasurface ($y = 659$ mm) as an example of the limiting case. The simulation results are shown in Figs. 4(c) and 4(d), where a larger focal region is observed with a smaller amplification factor of 1.64 at (506, 520) mm. The focusing performance decreases due to the limitation in the aperture size of the metasurface, which can be enhanced by increasing the number of the metasurface units.

To further demonstrate its versatility, the metasurface is used to guide the generated second-harmonic wave to propagate along a self-bending trajectory. To form a self-bending beam propagation, all the rays in the transmitted region should be tangent to the desired caustic trajectory.[20] Accordingly, the phase gradient profile of the metasurface can be determined via Legendre transform technique.[21] We design four metasurfaces to guide the SHG to propagate along different cubic caustic trajectories considering the aperture size. The resulting acoustic pressure fields are shown in Fig. 5, where the SHG is bent and propagates along the desired self-bending trajectory. Hence, the nonlinear acoustic metasurface does not only demultiplex different frequency components but also guide the SHG to propagate in any desired trajectory. Note that all the metasurface designs are achieved via tailoring middle mass value m_2, which can be realized by adding/subtracting additional mass units, enabling highly tunable nonlinear metasurface designs for various anomalous wave control.

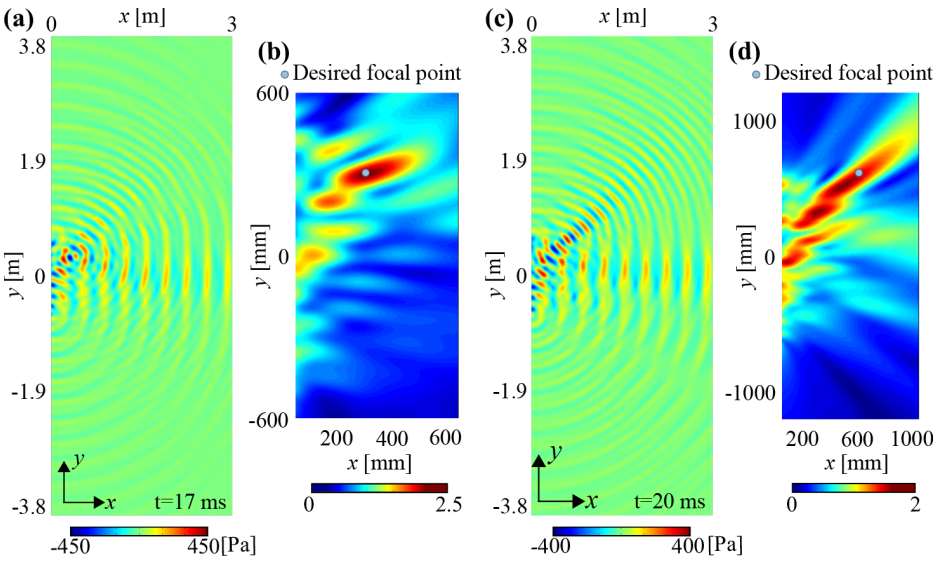

FIG. 4. Focusing metasurface designs with different desired focal points. (a) The transmitted acoustic pressure field and (b) normalized RMS pressure field of the focusing metasurface with desired focal point $(f_x, f_y) = (304.8, 304.8)$ mm. (c) The transmitted acoustic pressure field and (d) normalized RMS pressure field of the focusing metasurface with desired focal point $(f_x, f_y) = (609.6, 609.6)$ mm, close to the upper boundary of the metasurface.

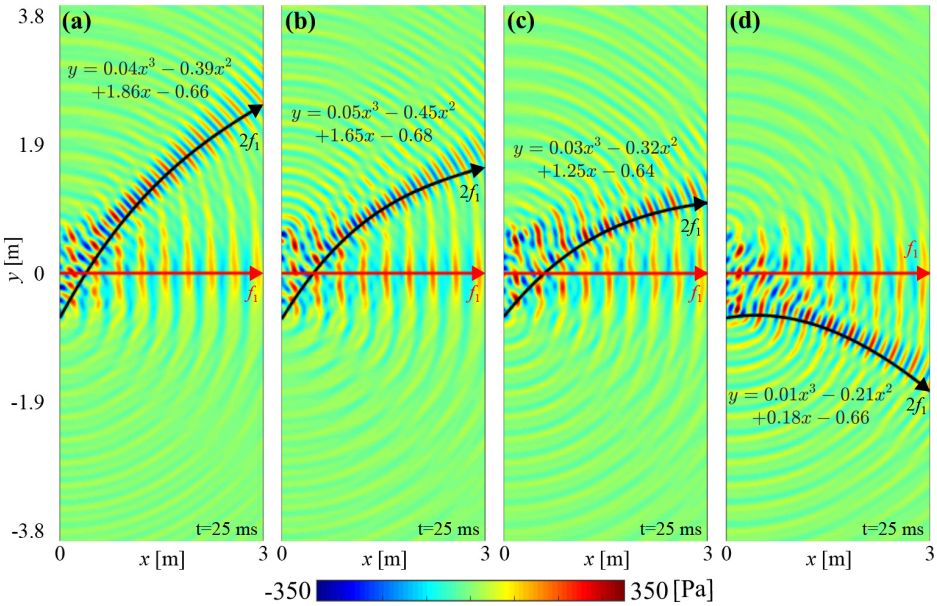

FIG. 5. The transmitted acoustic pressure fields of different self-bending beam propagation designs with desired trajectory: (a) $y = 0.04x^3 - 0.39x^2 + 1.86x - 0.66$, (b) $y = 0.05x^3 - 0.45x^2 + 1.65x - 0.68$, (c) $y = 0.03x^3 - 0.32x^2 + 1.25x - 0.64$, and (d) $y = 0.01x^3 - 0.21x^2 + 0.18x - 0.66$.

In summary, we propose and explore a nonlinear acoustic metasurface consisting of structural modules with curved beams to tailor and harness SHG for anomalous wavefront control. Our innovation and findings include (i) a nonlinear unit cell design for achieving significant SHG propagating into the transmission region, (ii) insight from amplitude-dependent analysis of transmission and phase modulation by tailoring the structural parameters of the proposed nonlinear unit cell, and (iii) design of nonlinear acoustic metasurfaces to demultiplex different harmonics and control the second-harmonic wavefront for diverse functions, including wave deflecting, wave focusing, and self-bending propagation. With the advanced theoretical, numerical, and experimental efforts, this study uncovers unconventional wave control via nonlinear metasurfaces and creates potential toward a broad range of engineering applications, e.g., phonon computing[22] and ultrasonic diagnosis and therapy in biomedicine, where higher-order harmonic generation can be harnessed to image smaller objects.[23]

See the supplementary material for more details on unit cell parameters, spring stiffness determination, and analytical formulation.

This work was supported by the National Science Foundation under Grant No. CMMI-1933436 and the Air Force Office of Scientific Research under Grant No. FA9550-21-1-0032.

AUTHOR DECLARATIONS

Conflict of Interest

The authors have no conflicts to disclose.

Author Contributions

Zhenkun Lin and Yuning Zhang contributed equally to this work.

Zhenkun Lin: Conceptualization (equal); Formal analysis (equal); Methodology (equal); Validation (equal); Writing – original draft (equal). **Yuning Zhang:** Conceptualization (equal); Formal analysis (equal); Methodology (equal); Validation (equal); Writing – original draft (equal). **Kon-Well Wang:** Funding acquisition (equal); Supervision (equal); Writing – review & editing (equal). **Serife Tol:** Funding acquisition (equal); Supervision (equal); Writing – review & editing (equal).

DATA AVAILABILITY

The data that support the findings of this study are available from the corresponding author upon reasonable request.

REFERENCES

[1]M. V. Barnhart, X. Xu, Y. Chen, S. Zhang, J. Song, and G. Huang, "Experimental demonstration of a dissipative multi-resonator metamaterial for broadband elastic wave attenuation," J. Sound Vib. **438**, 1–12 (2019).
[2]Z. Lin, H. Al Ba'ba'a, and S. Tol, "Piezoelectric metastructures for simultaneous broadband energy harvesting and vibration suppression of traveling waves," Smart Mater. Struct. **30**, 075037 (2021).
[3]S. Tol, F. L. Degertekin, and A. Erturk, "Phononic crystal Luneburg lens for omnidirectional elastic wave focusing and energy harvesting," Appl. Phys. Lett. **111**, 013503 (2017).
[4]G. Hu, L. Tang, J. Liang, C. Lan, and R. Das, "Acoustic-elastic metamaterials and phononic crystals for energy harvesting: A review," Smart Mater. Struct. **30**, 085025 (2021).
[5]P. Dorin and K. W. Wang, "Broadband frequency and spatial on-demand tailoring of topological wave propagation harnessing piezoelectric metamaterials," Front. Mater. **7**, 409 (2021).
[6]Z. Wu, Y. Zheng, and K. W. Wang, "Metastable modular metastructures for on-demand reconfiguration of band structures and nonreciprocal wave propagation," Phys. Rev. E **97**, 022209 (2018).
[7]Z. Wu and K. W. Wang, "On the wave propagation analysis and supratransmission prediction of a metastable modular metastructure for non-reciprocal energy transmission," J. Sound Vib. **458**, 389–406 (2019).
[8]B. Assouar, B. Liang, Y. Wu, Y. Li, J. C. Cheng, and Y. Jing, "Acoustic metasurfaces," Nat. Rev. Mater. **3**, 460–472 (2018).

[9]Y. Li, X. Jiang, R. Q. Li, B. Liang, X. Y. Zou, L. L. Yin, and J. C. Cheng, "Experimental realization of full control of reflected waves with subwavelength acoustic metasurfaces," Phys. Rev. Appl. **2**, 064002 (2014).
[10]S. A. Cummer, J. Christensen, and A. Alù, "Controlling sound with acoustic metamaterials," Nat. Rev. Mater. **1**, 16001 (2016).
[11]H. Zhu and F. Semperlotti, "Anomalous refraction of acoustic guided waves in solids with geometrically tapered metasurfaces," Phys. Rev. Lett. **117**, 034302 (2016).
[12]Y. Zhu, L. Cao, A. Merkel, S.-W. Fan, and B. Assouar, "Bifunctional superlens for simultaneous flexural and acoustic wave superfocusing," Appl. Phys. Lett. **116**, 253502 (2020).
[13]Z. Lin and S. Tol, "Elastic metasurfaces for full wavefront control and low-frequency energy harvesting," J. Vib. Acoust. **143**, 061005 (2021).
[14]J. Lan, Y. Li, Y. Xu, and X. Liu, "Manipulation of acoustic wavefront by gradient metasurface based on Helmholtz resonators," Sci. Rep. **7**, 1–9 (2017).
[15]B. I. Popa and S. A. Cummer, "Non-reciprocal and highly nonlinear active acoustic metamaterials," Nat. Commun. **5**, 1–5 (2014).
[16]X. Guo, V. E. Gusev, K. Bertoldi, and V. Tournat, "Manipulating acoustic wave reflection by a nonlinear elastic metasurface," J. Appl. Phys. **123**, 124901 (2018).
[17]X. Guo, V. E. Gusev, V. Tournat, B. Deng, and K. Bertoldi, "Frequency-doubling effect in acoustic reflection by a nonlinear, architected rotating-square metasurface," Phys. Rev. E **99**, 052209 (2019).
[18]T. J. Ypma, "Historical development of the Newton–Raphson method," SIAM Rev. **37**, 531–551 (1995).
[19]Y. F. Zhu, X. Y. Zou, R. Q. Li, X. Jiang, J. Tu, B. Liang, and J. C. Cheng, "Dispersionless manipulation of reflected acoustic wavefront by subwavelength corrugated surface," Sci. Rep. **5**, 1–12 (2015).
[20]L. Froehly, F. Courvoisier, A. Mathis, M. Jacquot, L. Furfaro, R. Giust, P. Lacourt, and J. Dudley, "Arbitrary accelerating micron-scale caustic beams in two and three dimensions," Opt. Express **19**, 16455–16465 (2011).
[21]P. Zhang, T. Li, J. Zhu, X. Zhu, S. Yang, Y. Wang, X. Yin, and X. Zhang, "Generation of acoustic self-bending and bottle beams by phase engineering," Nat. Commun. **5**, 1–9 (2014).
[22]S. R. Sklan, "Splash, pop, sizzle: Information processing with phononic computing," AIP Adv. **5**, 053302 (2015).
[23]O. V. Rudenko, "Giant nonlinearities in structurally inhomogeneous media and the fundamentals of nonlinear acoustic diagnostic techniques," Phys.-Usp. **49**, 69 (2006).